Journal of
Ceramic Science
and Technology

J. Ceram. Sci. Tech., **05** [01] 13-22 (2013)
DOI: 10.4416/JCST2013-00022
available online at: http://www.ceramic-science.com

Evaluating Porosity in Cordierite Diesel Particulate Filter Materials, Part 2 Statistical Analysis of Computed Tomography Data

Y. Onel, A. Lange, A. Staude, K. Ehrig, A. Kupsch, M.P. Hentschel, T. Wolk, B.R. Müller, G. Bruno*

BAM Federal Institute for Materials Research and Testing, D-12200 Berlin, Germany
received August 23, 2013; received in revised form October 18, 2013; accepted November 18, 2013

Abstract

Complementary to Part 1 of this work, the bi-continuous microstructure of porous synthetic cordierite ceramics for filtration applications was investigated using 3D x-ray computed tomography at different resolutions. Applying both Fast Fourier Transform and a newly developed image analysis algorithm, we quantitatively evaluated porosity and pore orientation. The statistical approach allows extraction of spatially resolved or average values. Porosity values based on x-ray absorption agree with mercury intrusion measurements, while pore orientation factors agree with x-ray refraction data (Part 1 of this work), and with published crystallographic texture data.

Keywords: Pore orientation, porous ceramics, computed tomography, 3D microstructure

I. Introduction

Porous synthetic cordierite has been successfully used as filtration material for over 20 years. Its major applications are discussed in several works [1,2]. Besides depending on the filter cell geometry, both the filtration performance and the mechanical properties of these materials strongly depend on their microstructure [3]. Particularly important are four factors: *i*) microcracking [4,5]; *ii*) porosity [5,6]; *iii*) crystallographic and *iv*) morphological texture (i.e. grain size and orientation) [7].

As mentioned in Part 1 of this work [8], and in [5,9], although texture factors of extruded monoliths are weak compared with metals, the preferential grain orientation is sufficient to bring about very low axial thermal expansion, and consequently high thermal shock resistance [10,11]. Microcracking strongly influences the thermo-mechanical properties (thermal expansion and conductivity, Young's modulus, strength, fracture toughness) [4,12,13,14], analogously to other similar ceramics (aluminum titanate [15,16], β-eucryptite [17]). As described in pioneering papers [18,19,20], the grain (or domain) size determines the onset of microcracking.

In general, porosity and pore morphology directly determine the effective mechanical properties of porous ceramics [21,22]. These bi-continuous materials are no exception. Furthermore, their filtration performance is also strongly affected by the pore morphology. This fact has motivated us to quantitatively characterize the pore orientation in a bi-continuous medium such as a DPF. In fact, it has been shown that porosity alone, while easily experimentally measureable by means of mercury intrusion or x-ray absorption [8], is not sufficient for a thorough description of the material's microstructure. Moreover, other information is needed, e.g., on the pore shape and/or orientation, in order to evaluate the influence of the pore structrure on the material's properties. On top of this consideration, intrusion techniques (mercury [23,24], gas and water [25]) assume cylindrical pore shapes. They can therefore be used in relatively simple cases (see [26]), but the assumption of cylindrical pore shape is unacceptable in bi-continuous media with almost exclusively open porosity, and even in simpler cases such as that of hollow spheres [27]. Therefore, imaging methods have been used. Several authors have used SEM image analysis to determine porosity in similar materials: Gordon *et al.* [6], Sandoval *et al.* [28], Živcová-Vlčková *et al.* [29] have used binarization of 2D images and compared them with mercury intrusion to determine porosity. SEM images suffer from the classic limitation of being two-dimensional: stereological corrections (see e.g. [27]) cannot apply in the case of complex and irregular pore morphologies. Furthermore, SEM Images offer a limited field of view (FoV), whose statistical significance can always be questioned. Neutron tomography [30] was applied to investigate entire DPFs [31,32], but with very limited spatial resolution [33]. This prevented detailed investigation of the pore structure. The use of 3D tomograms [25,34] is obviously a modern way to tackle the problem. However, the decisive factor for success in the determination of pore orientation is the algorithmic approach to *quantitative* microstructural determination. Both SEM and tomography images are typically evaluated by fitting known shapes (ellipsoids and spheres [35]) to the measured microstructure, in order to extract morphological texture (see for example [36]). A statistical analysis of CT data would be much more powerful, as it would be free from unnecessary hypotheses. Indeed, this approach has been proposed

* Corresponding author: giovanni.bruno@bam.de

by Zhao *et al.* [37] to calculate filter permeability. These authors used skeletonization to calculate the permeability, instead of solving the Navier-Stokes equation based on FEM. In our context, more directed at the calculation of thermal and mechanical properties, we focus on the evaluation of the pore orientation, which is an overall microscopic property that directly influences thermal expansion and Young's modulus (see [4, 38, 39]). We present simple statistical methods to analyze 3D CT data, and show that the results of statistical calculations fully agree with data available in the public literature.

II. Materials and Experimental Methods

(1) Materials

Two commercial cordierite DPF ceramic honeycomb filter materials were used in this work. Small samples for x-ray tomography experiments were extracted from larger pieces (see Part 1 of this work). The honeycomb materials were cordierite-based, produced by means of extrusion of a mixture of talc, kaolin, alumina, silica, and pore formers, and firing at a temperature in excess of 1400 °C. For the details of the sample characterization the reader is referred to Part 1 of this work [8] and to previous works [4, 40, 41, 42]. For convenience, some sample properties are given again: sample S1 has a porosity of 62 % and median pore size of 10 μm, while S2 exhibits 50 % porosity and 18 μm median pore size, as determined by means of mercury intrusion.

The high spatial resolution of modern computed tomography in the range of (optical) microscopic imaging provides the opportunity of both: detailed 3D imaging and nondestructive handling of the highly porous fragile ceramics, free from preparation artifacts (e.g., by polishing in the case of microscopy). Computed tomography was therefore used at two different levels of resolution: μCT on laboratory equipment, revealing details on the 10 μm scale, and synchrotron CT, in order to achieve higher spatial resolution (about 0.4 μm).

(2) μ-Computed tomography

Laboratory μ-CT experiments were performed on a v|tome|x L 300/180 (GE Inc.) x-ray tomography system, operated at U = 60 kV, I = 150 mA. The nanofocus tube contains a tungsten transmission target with an actual focal spot size below 2 μm (determined with JIMA test pattern RTC02). The sample was placed 17.5 mm downstream of the source. With a focus-detector distance of 1000 mm, the effective magnification on the 2000 × 2000 pixel DXR-250 detector (GE Inc.) amounts to 57.1, corresponding to an effective pixel size of 7 μm. The sample projections were taken at 1440 angular position, with increments of 0.25°, and an exposure time of 3 seconds. In order to ensure the projection of the entire sample, pieces of 2 × 2 cells were cut out of the honeycomb assemblies (Fig. 1).

(3) Synchrotron radiation computed tomography

Synchrotron-CT measurements were performed at the beamline BAM*line* [43, 44] at the synchrotron source BESSY II of the Helmholtz-Zentrum Berlin für Materialien und Energie (HZB), Berlin, Germany.

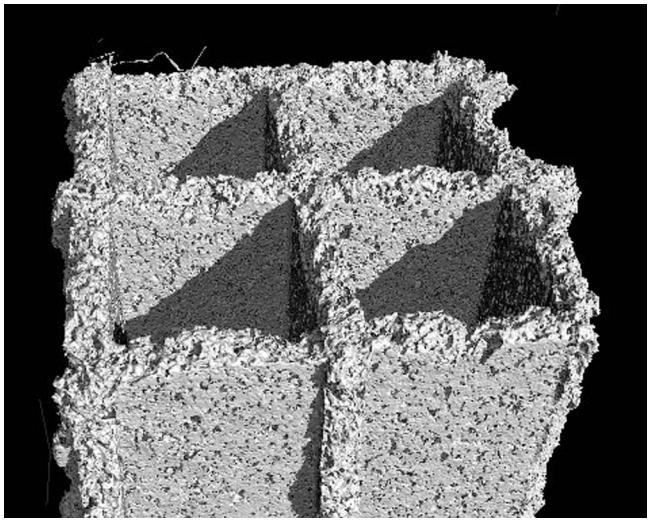

Fig. 1: 3D rendered image of the laboratory μCT reconstruction of sample S2.

An Optique Peter microscope was used in combination with a $CdWO_4$ scintillator, a 10-fold magnifying objective and a pco.4000 CCD camera (4008 × 2672 pixels). The resulting pixel size was 0.434 μm.

The beam energy was adjusted to 15 keV, in order to achieve optimum contrast for the investigated pore structures. The entrance slits were narrowed to the FoV (1.7 ×1.1 mm^2) in order to avoid detector backlighting [45, 46]. 3200 single projections were collected in an angular sector of 180° at 4 s exposure.

The small sample-detector distance of 15 mm ensured a limited scattering range of refractive edge artifacts. The resulting modulation of the attenuated intensity was subjected to a "phase-retrieval" filter, applying the ANKAphase algorithm [47], with a δ/β ratio of 20 (δ and β being the real and imaginary part of the x-ray refraction index $n = 1 - \delta - i\beta$).

In order to avoid the sample size exceeding the FoV, small splinters of less than 1.5 mm size were prepared from each sample, containing just one crossing region and one protruding wall (see Fig. 2).

III. Procedures for Pore Orientation Analysis

Two alternative approaches to pore orientation analysis were used. They both aimed at avoiding unnecessary hypotheses on the pore shape (typical of conventional porosity analysis tools). This was particularly important in our case, where closed porosity plays a negligible role. The applied techniques yield (from 2D images) integral information on the homogeneity and on the degree of anisotropy of these materials: The new technique of DIVA (directional interface variance analysis) represents a statistical approach to the extraction of quantitative information from 2D images, while the Fourier technique of periodograms [48] is sensitive to pore size and orientation distribution. Both were applied to thin slices of 3D CT reconstructions parallel to the extrusion direction.

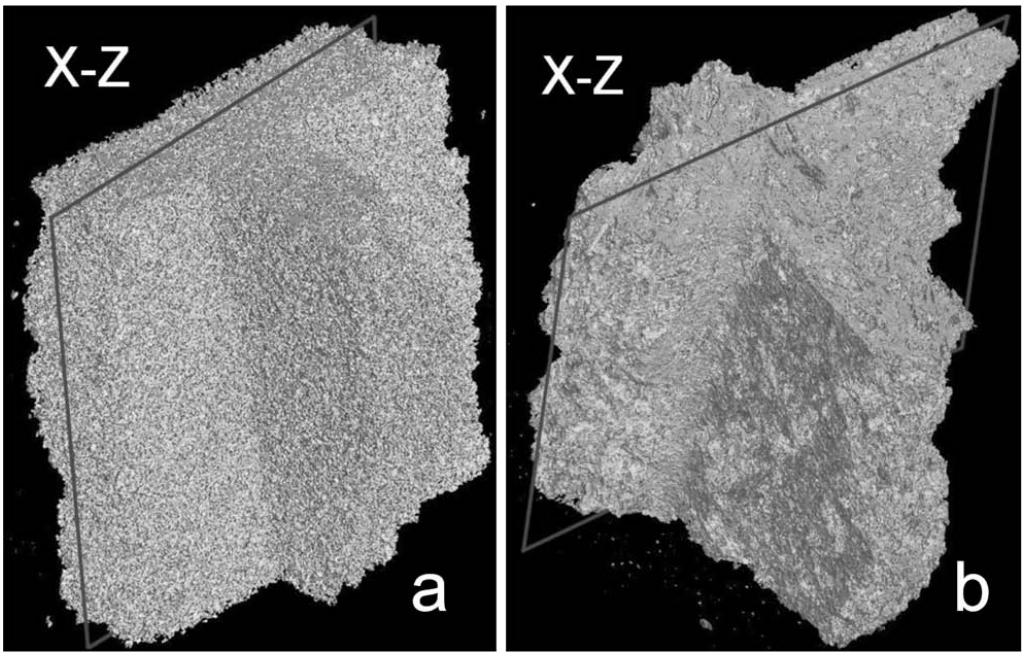

Fig. 2: 3D rendered views of sample S1 and S2 (a and b) with indicated orientation of X-Z planes (synchrotron data).

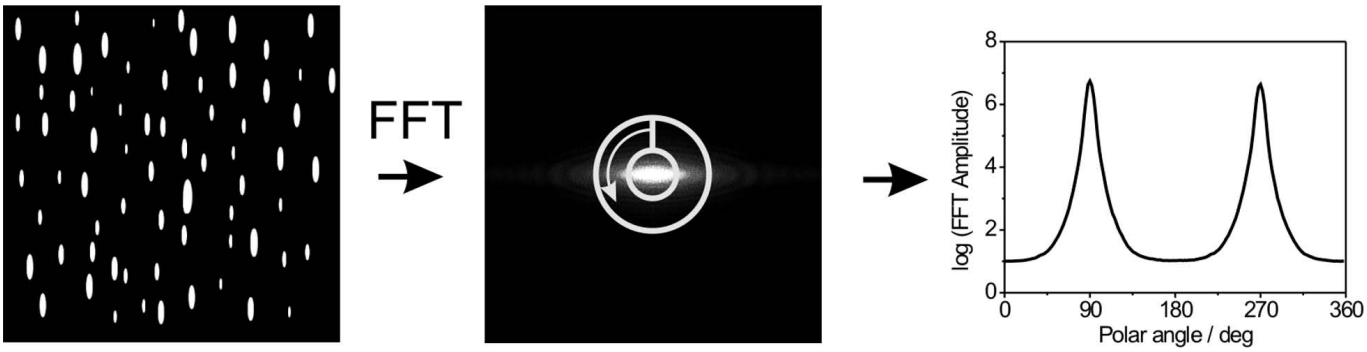

Fig. 3: The principle of FFT periodogram analysis; left: anisotropic model structure, center: Fourier magnitude image with indicated radial range of the polar angle sampling; right: resulting polar angle plot.

(1) FFT analysis

In a first approach, FFT analysis of 2D slices was performed with periodograms [48]. The 2D Fourier amplitude contour plots of the tomographic sections were evaluated plotting the amplitude *vs*. the polar angle, integrating over a selected radial range (see Fig. 3). This is illustrated in Fig. 3 for a model case of aligned elliptical objects. The Fourier transform and the respective polar plot are also shown. The latter plot *quantitatively* indicates the preferred direction as well as the degree of anisotropy by means of the peak positions and heights. It should be noted that the FFT is also sensitive to the object size: large objects (small spatial frequencies) are concentrated at the center, small objects are spread to larger radii in the FFT image. This implies that we perform an unknown weighted averaging over the different pore sizes present in the sample. Thus, the amplitudes of the resulting polar plot strongly depend on the radial range of integration. In order to minimize this uncertainty, a radial range that is as large as possible should be chosen, thereby averaging over the largest possible population distribution section. An alternative method, not subject to this pitfall, was developed.

(2) DIVA: Directional interface variance analysis

The principles of directional interface variance analysis (DIVA) apply to every anisotropic microstructure, without any assumption regarding the lateral separability of close 'defects' (pores or particles).

From a given slice of a 3D CT image, a square area is selected (Fig. 4a). Within this (2D) selection, we compute the absolute values of the specific mass (or attenuation coefficient) gradients $|\nabla\mu(\mathbf{r})|$ at all points **r**. These gradients are then binarized with an appropriate threshold. While keeping the selection fixed, the area is projected under several angles φ (i.e., integrated along η and sampled along ξ, see Fig. 4b). Thus we obtain the 1D projection $P_\varphi(\xi)$ expressed as

$$P_\varphi(\xi) = \int_V |\nabla\mu(r)| d\eta \qquad (1)$$

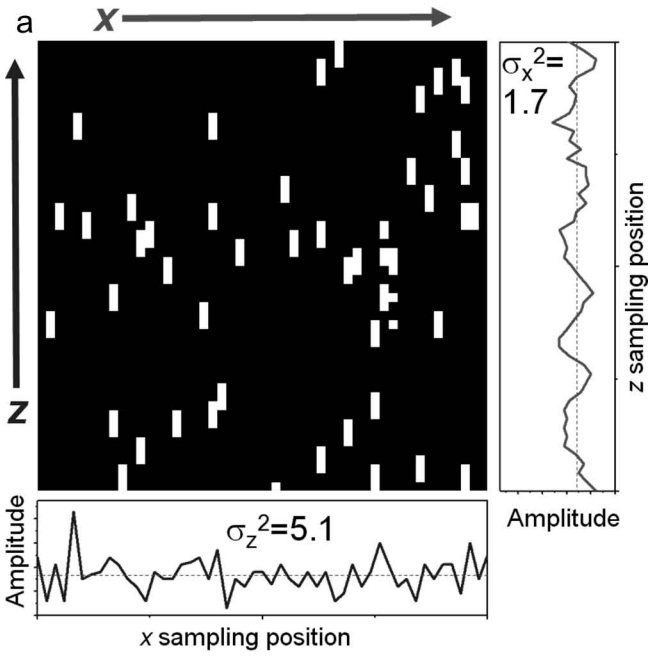

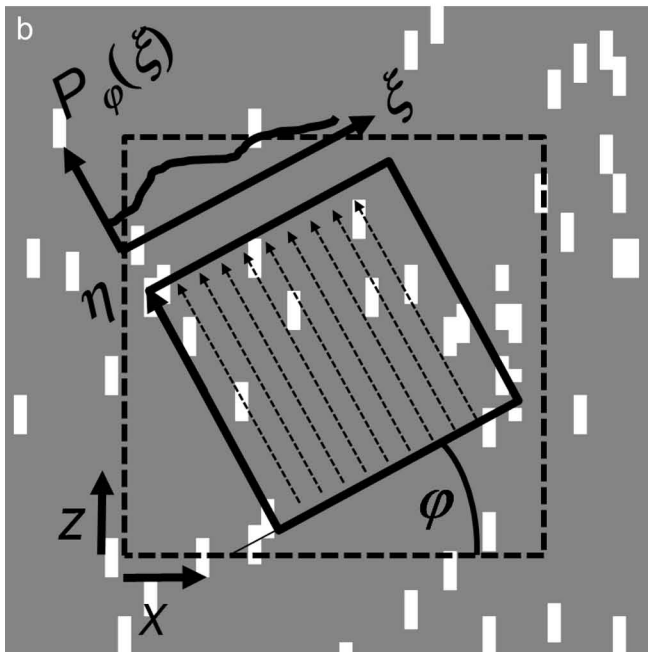

Fig. 4: The principle of DIVA (directional interface variance analysis); (a) random pixel pattern elongated along the vertical *z*-direction by a factor of 3. Bottom and right: projections along the z- and x-direction and the respective variances σ^2, equal to 5.1 and 1.7, respectively, (b) same pattern but the projection direction is rotated by an angle φ with respect to the x-axis.

The relation between coordinates $\mathbf{r} = (x, z)$ in the original and in the rotated coordinate system $\mathbf{r'} = (\eta, \xi)$ (Fig. 4b) is defined by a conventional rotation matrix. From each projection we determine the variance

$$\sigma_P^2(\varphi) = \left[\sum_{\xi_i}^{n} \left(P_\varphi(\xi_i) - \langle P_\varphi \rangle \right)^2 \right] / n \qquad (2)$$

by integrating over all coordinates ξ (discretized as n points ξ_i in Eq.(2)). Here $\langle P_\varphi \rangle$ is the mean value of $P_\varphi(\xi_i)$ and n is the number of sampling points (i.e., the number of pixels in the 1D projection).

The reason for choosing the absolute value of gradients instead of the attenuation coefficient (or mass distribution) is to gain relevant information about the pore/particle interface orientation. It can be observed that within highly porous materials, 1D projections of the attenuation coefficient would cause a considerable overlap of pore areas. This overlap would reduce the variance of projections and therefore their sensitivity to anisotropy.

The minimum ratio between two variances in perpendicular projections defines an orientation parameter O_D. This is equal to unity in case of isotropic patterns, otherwise, it is a quantitative measure of the preferred orientation of the investigated objects (in our case, the pores).

The procedure described above is sketched in Fig. 4a for the ideal case of elongated objects, represented by pixels with finite size. A random pixel pattern is elongated by a factor of k (=3) along a unique direction (here: the vertical z-direction). The projection (line integral) along this direction reveals a variance that is exactly k times larger than the variance in the perpendicular direction. Rotating the projection directions of the pattern as a function of the angle φ (Fig. 4b) results in decreasing variance ratios, until the minimum (inverse) ratio is reached for a 90° rotation. For further rotations, the ratios of variances is simply reversed: a maximum is reached at φ = 180°, and a minimum at φ = 270°. Thus, identifying the maximum value of the variance ratio as a function of the polar angle provides both the preferential direction (the angular position of the maximum), and a quantitative measure of the anisotropy (the amplitude of the maximum and/or minimum). We will call this diagram the variance ratio polar plot in the rest of the text.

IV. Results and Discussion

(1) CT results

The (*laboratory*) μ-CT 3D reconstruction of the spatial mass distribution of the DPF samples was performed using a standard Feldkamp-David-Kress algorithm (Figs. 5 represent cross-sections perpendicular to the extrusion axis, Fig. 6 represents a cut within the wall plane) [49].

The *synchrotron* CT data were reconstructed with the BAM implementation of the standard filtered back-projection algorithm (Fig. 7), using a ramp-filter.

As a pre-check, the relative mass occupancy was determined as a function of depth position within the walls. No significant variation was observed in both samples and in both orientations. The integral values of porosity determined by image analysis of reconstructed slices from synchrotron results were 65 % (±1 %) for sample S1 and 52 % (±2 %) for sample S2. This is in very good agreement with the porosity determined with mercury intrusion (62 % and 50 %, respectively).

As can be seen from Figs. 5 to 7, the majority of pores is open at all lengthscales. The application of any standard pore/particle analysis software tool (based on the identification of individual closed pores) would fail to yield reliable results. The quantitative evaluation of CT reconstructions therefore requires an approach that is preferably independent of shape, size and connectivity.

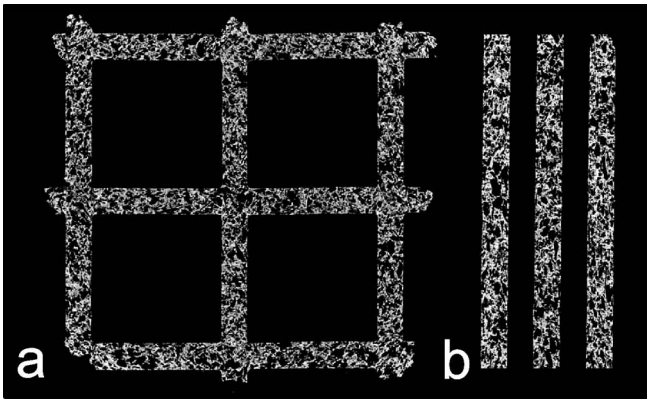

Fig. 5: Reconstructed slices of the 4-cell sample (S2) measured by μ-CT: (a) transverse cross-section; (b) overlap of wall cross sections (not containing crossings).

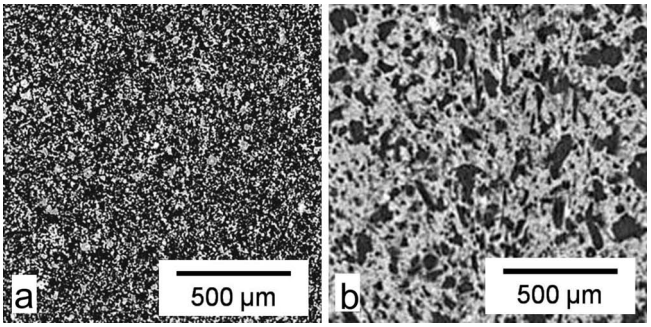

Fig. 6: Laboratory μCT reconstruction details of wall structures (200 × 200 pixel or 1.4 × 1.4 mm^2) of samples S1 (a) and S2 (b), cut in the X-Z plane.

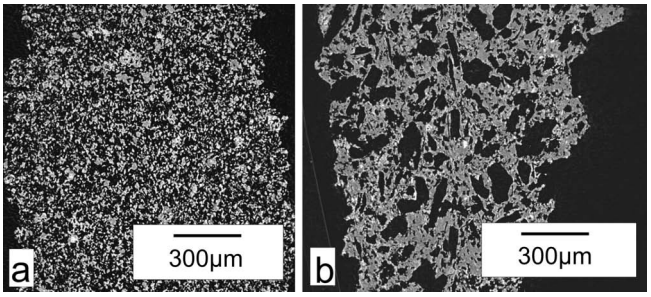

Fig. 7: Arbitrarily chosen X-Z slices of synchrotron CT images (coordinates see Fig. 2) of samples S1 (a) and S2 (b), with the Z direction (extrusion) vertical.

(2) FFT analysis

For direct visualization of the preferred pore orientation Fig. 8 shows a binarized slice of sample S2 reconstruction obtained from μCT (Fig. 8a) and the corresponding FFT magnitude (Fig. 8b). The difference between the Fourier transforms of the slice in Fig. 8a and of its 90° rotated copy amplifies the perceptibility of the pore preferred orientation along the extrusion direction (Fig. 8c).

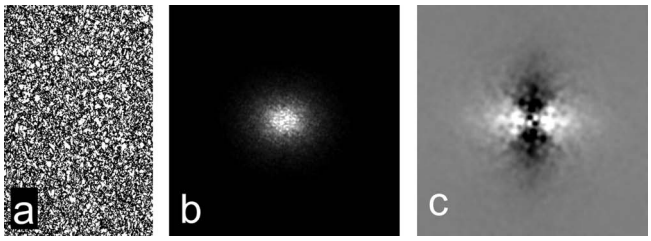

Fig. 8: Direct visualization of preferred pore orientation by the difference of Fourier transforms; (a) binarized inverted pore image; (b) its FFT (logarithmic power spectrum); (c) difference image (see text).

In addition, using reconstruction slices of synchrotron data such as those illustrated in Fig. 7, we can gain information about the depth dependence of these orientations within the cordierite wall. The FFT analysis of a statistically representative fraction of sample S2 (Fig. 9, left) yields polar profiles, as described in section III*(2)*: The FFT magnitude is integrated over different radii (Fig. 9, center), and yields a function of orientation angle (Fig. 9, right). The procedure can be applied to slices at different depths across the wall thickness. If we plot every integrated FFT magnitude graph as a function of orientation angle as gray values on a single (vertical) line, and then we stack (horizontally) lines corresponding to different depths, we obtain the image in Fig. 10. This figure shows that the preferential orientation maximum at 0° (i.e. the extrusion direction), indicated by the dashed line, is virtually the same throughout the whole wall thickness.

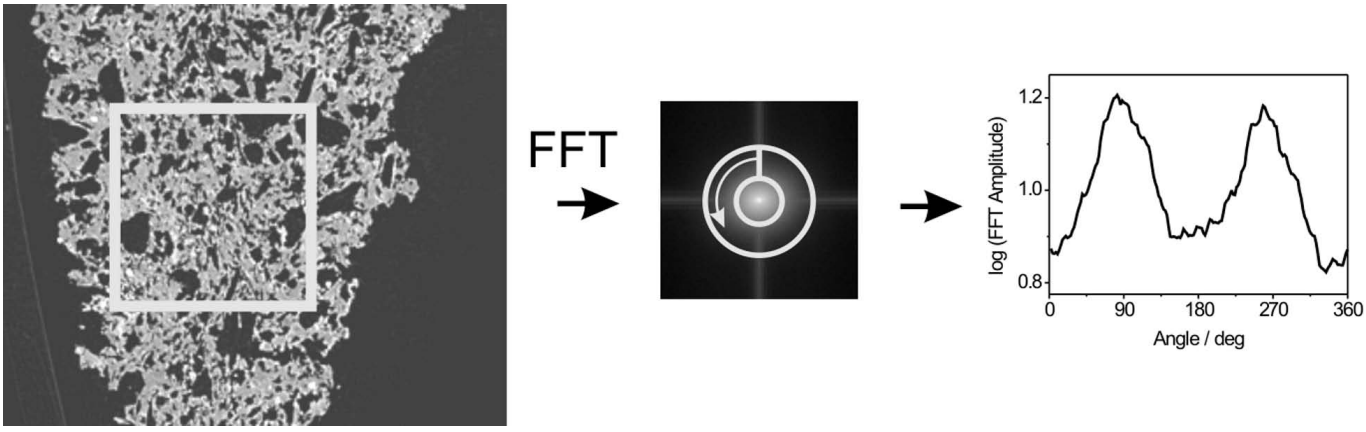

Fig. 9: Principle of FFT analysis. A representative fraction of a reconstructed slice (left) is Fourier transformed. Polar FFT profiles are integrated over several radii (center), and then plotted as a function of orientation angle (right).

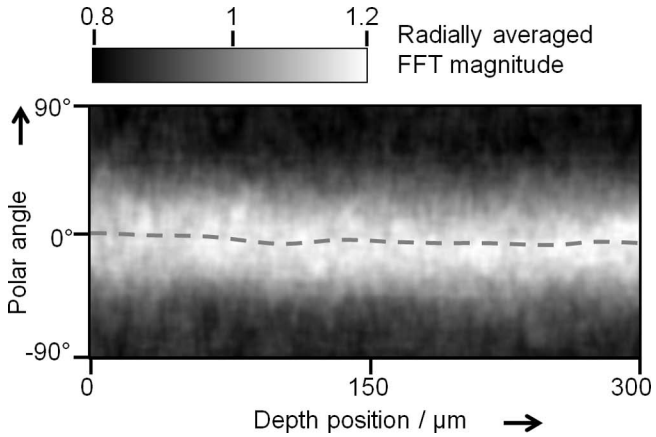

Fig. 10: FFT analysis applied to 2D slices taken at different depth positions across the wall thickness. The radially integrated polar plots are represented in the interval [-90°, 90°] (relative to the extrusion direction) on single vertical lines as gray levels, and then stacked horizontally. The result is a gray value image of the orientation distribution as a function of depth in the cell wall. The maximum position is indicated by a dashed line (guide for the eye).

As mentioned before, the result of this polar analysis is dependent on the selection of the radial range (indicated in Fig. 9, center). Each radius in the reciprocal space (Fourier transformed) corresponds to a different pore size. Consequently, the method above integrates over several pore sizes. This implies that results are, strictly speaking, only qualitative. They help visualizing orientation effects, and can well approximate the average orientation with the proper choice of the radial integration range.

(3) DIVA

In order to quantitatively measure the preferred orientation of pore/particle interfaces, and the degree of their orientation, the directional interface variance analysis (DIVA) was applied to selected slices of the µCT reconstructions. Fig. 11a shows such an area (within sample S2) and the square region selected for the analysis. Fig. 11b displays DIVA variance ratio polar plots (limited between -90° and 90°) for samples S1 and S2. We notice an approximately 10 % higher degree of orientation for the coarser structure of sample S2. Table 1 lists the minimum variance ratios of the two filter materials averaged over 26 single slices within each wall.

Analogous to Fig. 10, Fig. 12 shows a typical orientation parameter profile (again in gray levels) across a wall thickness, generated by stacking (horizontally) the variance ratio polar plots, and using the high resolution synchrotron CT data. Contrary to Fig. 10, we observe in this case considerable changes in the preferred orientation direction of the pore edges as a function of thickness. These variations are of about ±10°.

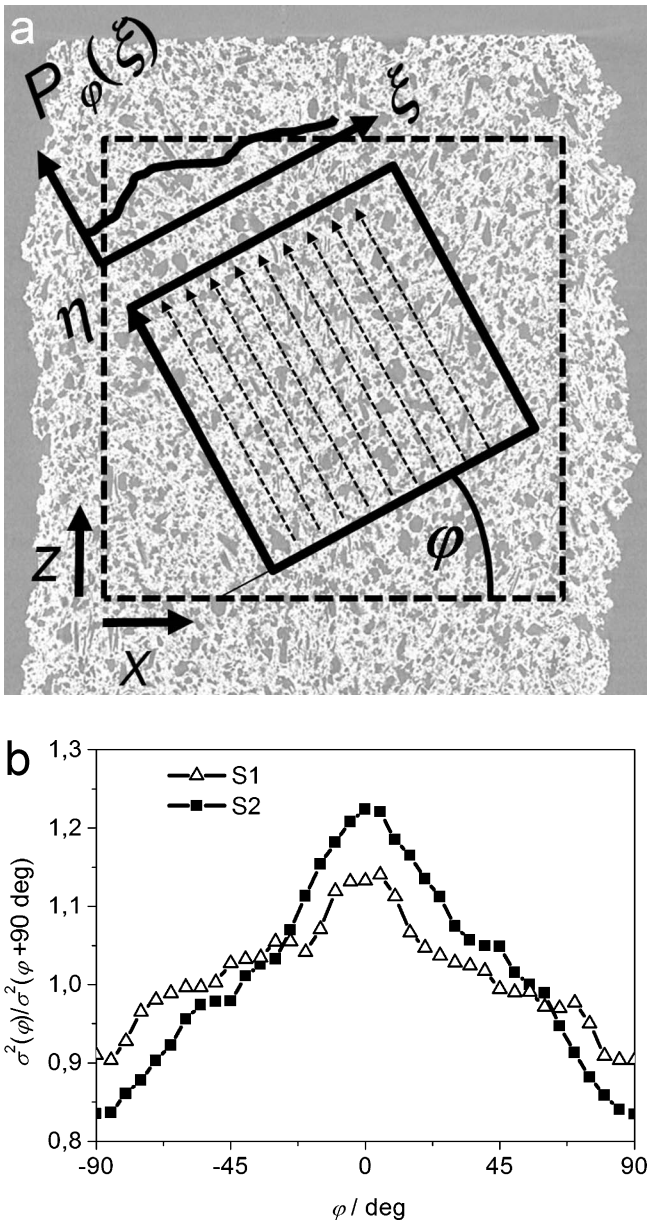

Fig. 11: Application of the DIVA technique to cordierite samples; (a) the full square inside the inspection area (dashed square) indicates the region used for calculation of the variance; (b) polar plots of the ratios of variances (averaged across the wall) in orthogonal directions. The results can immediately be read from the minimum values.

Table 1: Results of DIVA applied to µ-CT and synchrotron CT reconstructions and comparison with the x-ray refraction results reported in Part 1 of this work.

	X-ray Refraction	µ-CT: minimum variance ratio (‖/⊥)	Synchrotron CT: walls	Synchrotron CT: crossings	Synchrotron CT: crossings/walls ratio
S1	0.92	0.92	0.85	0.77	0.91
S2	0.86	0.84	0.74	0.61	0.83

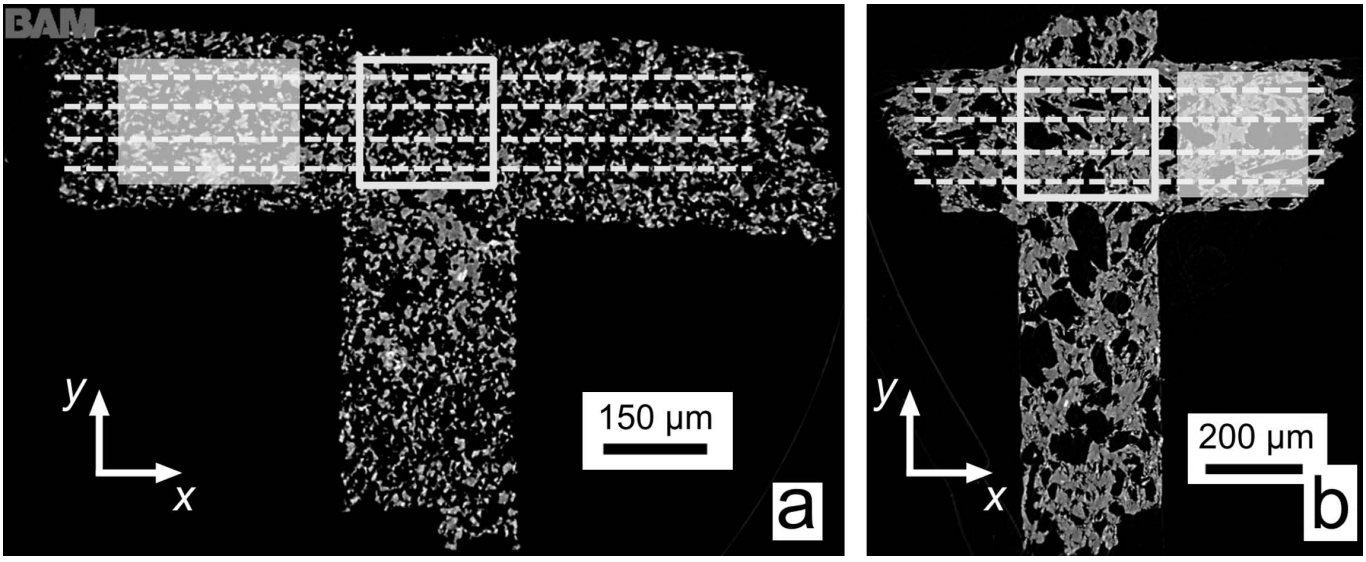

Fig. 13 : Selected volumes for the application of DIVA at different depths, separating partial volumes in the walls (shaded boxes) and crossings (open boxes) of samples S1 (a) and S2 (b). The traces of X-Z planes are indicated as dashed lines.

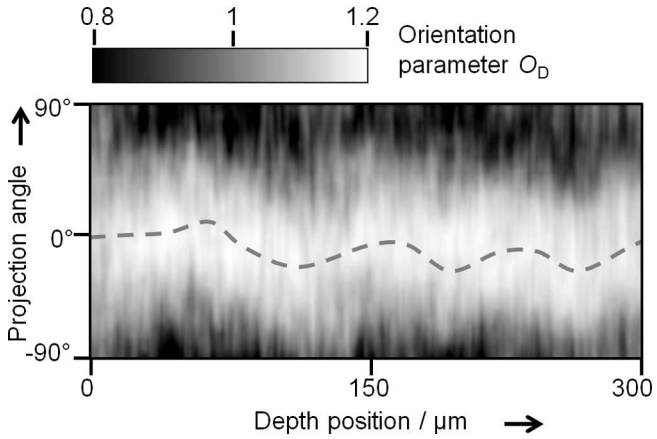

Fig. 12 : DIVA profile generated by stacking (horizontally) the variance ratio polar plots at different depth positions across the wall. The polar plots are collapsed on single vertical lines and represented by means of gray levels. Comparing to the FFT analysis of Fig. 10 much larger deviations from 0 degree can be observed. The maximum position is indicated by a dashed line (guide for the eye).

The discrepancy with the µ-CT results (Fig. 10) can be explained by the different resolutions and investigated volumes (larger volume and coarser resolution for the laboratory µCT data). The two datasets are therefore complementary, and, indeed, the higher spatial resolution of the synchrotron CT data turns out to be of great advantage if we want to investigate the orientation differences between walls and crossings. The segmentation of the two different spatial regions is sketched in Fig. 13. Also in those regions the DIVA amplitudes and maxima positions vary as a function of depth. A separate analysis of the walls and the crossings shows significant differences (Table 1). The ratios of the DIVA minima within walls and crossings (averaged over the entire wall thickness) are 0.91 ± 0.02 for S1 and 0.83 ± 0.02 for S2. This proves that a higher degree of pore orientation is present in the crossing volumes for both materials.

The variance ratio for both the walls and the crossings slightly deviate from those determined with µ-CT on the whole structure. This can be explained by the different resolution: the higher resolution (16 ×) of synchrotron data allows imaging smaller (oriented) pores, which otherwise look isotropic in a coarser dataset.

Table 1 summarizes all quantitative results: the minimum variance ratios determined by DIVA on µ-CT and synchrotron data agree very well with each other. Moreover, CT results are in accordance with our findings from x-ray refraction analysis (Part 1 of this paper).

V. Summary and Conclusions

Complementary to the x-ray refraction approach used in Part 1 of this work, we have used laboratory and synchrotron CT data to gain quantitative microstructural information about the porous structure of two synthetic cordierite materials. Statistical evaluation tools have been used to analyze porosity and pore orientation. The well-established FFT technique (in the form of the so-called periodograms) revealed that the preferred pore direction is parallel to the extrusion direction. With the use of high-resolution (synchrotron) CT data we found that the pore orientation varies considerably as a function of depth, and when moving from walls to crossings. In addition, we developed an alternative technique that allowed us to cast light on the angular orientation distribution of pore interfaces. This statistical procedure (DIVA, directional interface variance analysis) does not require any assumption regarding shape and size of pores or particles. By means of the calculation of variance ratios of orthogonal projections of gradient images, we could obtain 1D polar plots analogous to texture pole figures. These variance polar plots give a quantitative measure of the deviations (angular positions and intensity) from random orientation, and agree very well with results from previous experimental work (including our own). Orientation factors agree well with the crystallographic texture data reported in the literature. This underlines the intimate link between the crystallographic and the morphological texture of these materials.

Acknowledgments

Amit Shyam (Oak Ridge National Laboratory), and Randy Stafford (Cummins Inc.) kindly provided the DPF sample.

References

1 Readey, M.J., Rontanini, L.D.: Cordierite material useful in a heat source retainer and process for making the same. US Patent 4973566, (1990).

2 Saito, N., Nishimura, S.-Y., Kawano, M., Araki, S.-I., Sukenaga, S., Nakashima, K., Yasukouchi, T.: Fabrication of nitrogen-containing cordierite ceramics, *J. Am. Ceram. Soc.*, **93**, 2257 – 2263, (2010).

3 Merkel, G., Beall, D., Hickman, D., Vernacotola, M.: Effects of microstructure and cell geometry on performance of cordierite diesel particulate filters, SAE Technical Paper 2001 – 01 – 0193, 2001, doi:10.4271/2001 – 01 – 0193.

4 Shyam, A., Lara-Curzio, E., Pandey, A., Watkins, T.R., More, K.L.: The thermal expansion, elastic and fracture properties of porous cordierite at elevated temperatures, *J. Am. Ceram. Soc.*, **95**, 1682 – 1691, (2012).

5 Bruno, G., Efremov, A.M., An, C.P., Wheaton, B.R., Hughes, D.J: Connecting the macro and microscopic strain response in porous ceramics, Part II - Microcracking, *J. Mater. Sci.*, **47**, 3674 – 3689, (2012).

6 Gordon, T., Shyam, A., Lara-Curzio, E.: The relationship between microstructure and fracture toughness for fibrous materials of diesel particulate filters, *J. Am. Ceram. Soc.*, **93**, 1120 – 1126, (2010).

7 Bubeck, C.: Direction dependent mechanical properties of extruded cordierite honeycombs, *J. Eur. Ceram. Soc.*, **29**, 3113 – 3119, (2009).

8 Kupsch, A., Lange, A., Hentschel, M.P., Onel, Y., Wolk, T., Staude, A., Ehrig, K., Müller, B.R., Bruno, G.: Evaluating porosity in cordierite-based diesel particulate filter materials. Part 1 X-Ray Refraction. submitted to *J. Ceram. Sci. Techn.* (2013).

9 Bruno, G., Vogel, S.: Calculation of the average coefficient of thermal expansion in oriented cordierite polycrystals, *J. Am. Ceram. Soc.*, **91**, 2646 – 2652, (2008).

10 Kingery, W.D.: Factor affecting thermal stress resistance of ceramic materials, *J. Am. Ceram. Soc.*, **38**, 3 – 15, (1955).

11 Lachman, I.M., Bagley, R.D. and Lewis, R.M.: Thermal expansion of extruded cordierite ceramics, *J. Am. Ceram. Soc.*, **60**, 202 – 205, (1981).

12 Bruno, G., Kachanov, M.: On modeling of microstresses and microcracking generated by cooling of polycrystalline porous ceramics, *J. Eur. Ceram. Soc.*, 33, 1995 – 2005, (2013).

13 Bruno, G., Kilali, Y., Efremov, A.M.: Impact of the non-linear character of the compressive stress-strain curves on thermal and mechanical properties of porous microcracked ceramics, *J. Eur. Ceram. Soc.*, **33**, 211 – 219, (2013).

14 Bruno, G., Kachanov, M.: Porous microcracked ceramics under compression: micromechanical model of non-linear behavior, *J. Eur. Ceram. Soc.*, 33, 2073 – 2085, (2013).

15 Bruno, G., Efremov, A.M., Wheaton, B.R., Bobrikov, I., Simkin, V.G., Misture, S.:. Micro- and macroscopic thermal expansion of stabilized aluminum titanate, *J. Eur. Ceram. Soc.*, **30**, 2555 – 2562, (2010).

16 Bruno, G., Efremov, A.M., Webb, J.E.: The correlation between the coefficient of thermal expansion and the lattice mechanical properties of aluminum titanate, *Acta Mater.*, **58**, 6649 – 6655, (2010).

17 Bruno, G., Garlea, V.O., Muth, J., Efremov, A.M., Watkins, T.J., Shyam, A.: Temperature dependent microstress evolution in microcracked β-eucryptite, *Acta Mater.*, **60**, 4982 – 4996, (2012).

18 Cleveland, J.J., Bradt, R.C.: Grain size/microcracking relations for pseudobrookite oxides, *J. Am. Ceram. Soc.*, **61**, 478 – 481, (1978).

19 Ohya, Y., Nakagawa, Z.: Measurement of crack volume due to thermal expansion anisotropy of aluminum titanate ceramics, *J. Mater. Sci.*, **31**, 1555 – 1559, (1996).

20 Ohya, Y., Takahashi, Y., Nakagawa, Z.: Thermal expansion of grain boundary cracked aluminum titanate, *J. Mater. Sci.*, **31**, 1361 – 1365, (1996).

21 Gibson, L.J., Ashby, M.F.: The mechanics of three-dimensional cellular materials, *P. Roy. Soc. Lond. A Mat.*, **382**, 43 – 59, (1982).

22 Bruno, G., Efremov, A.M., Levandovsky, A.N., Clausen, B.: Connecting the macro and microscopic strain response in porous ceramics: modeling and experimental validation, *J. Mater. Sci.*, **46**, 161 – 173, (2011).

23 Lucas, R.: On the time-law of the capillary rise of liquids, (in German), *Kolloid Z.*, **23**, 15 – 22, (1918).

24 Washburn, E.W.: The dynamics of capillary flow, *Phys. Rev.*, **17**, 273 – 283, (1921).

25 Andersson, L., Larsson, P.T., Wågberg, L., Bergström, L.: Evaluating pore space in macroporous ceramics with water-based porosimetry, *J. Am. Ceram. Soc.*, **96**, 1916 – 1922, (2013).

26 Suzuki, Y., Kondo, N., Ohji, T., Morgan, P.E.D.: Uniformly porous composites with 3-D network structure (UPC-3D) for high-temperature filter applications, *Int. J. Appl. Ceram. Tech.*, **1**, 76 – 85 (2004).

27 Park, J.K., Lee, J.S., Lee, S.I.: Preparation of porous cordierite using gelcasting method and its feasibility as a filter, *J. Porous Mat.*, **9**, 203 – 210, (2002).

28 Sandoval, M.L., Camerucci, M.A., Tomba-Martinez, A.G.: High temperature mechanical behavior of cordierite-based porous ceramics prepared by modified cassava starch thermogelation, *J. Mater. Sci.*, **47**, 8013 – 8021, (2012).

29 Živcová-Vlčková, Z., Locs, J., Keuper, M., Sledlářová, I., Chmelíčková, M.: Microstructural comparison of porous oxide ceramics from the system, Al_2O_3-ZrO_2 prepared with starch as a pore-forming agent, *J. Eur. Ceram. Soc.*, **32**, 2163 – 2172, (2012).

30 Kardjilov, N., Manke, I., Hilger, A., Strobl, M., Banhart, J.: Neutron imaging in materials science, *Materials Today*, **14**, 248 – 256, (2011).

31 Manke, I., Strobl, M., Kardjilov, N., Hilger, A., Treimer, W., Dawson, M., Banhart, J.: Investigation of soot sediments in particulate filters and engine components. *Nucl. Instrum. Meth. A*, **610**, 622 – 626, (2009).

32 Strobl, M., Treimer, W., Ritzoulis, C., Wagh, A.G., Abbas, S., Manke, I.: The new V12 ultra-small-angle neutron scattering and tomography instrument at the Hahn-Meitner-Institut, *J. Appl. Crystallogr.*, **40**, 463, (2007).

33 Williams, S.H., Hilger, A., Kardjilov, N., Manke, I., Strobl, M., Douissard, P.A., Martin, T., Riesemeier, H., Banhart, J.: Detection equipment for micro imaging with neutrons, *J. Instrumentation*, **7**, 1 – 25, (2012).

34 Voigt, C., Jäckel, E., Aneziris, C.G., Hubálková, J.: Investigations of reticulate porous alumina foam ceramics based on different coating techniques with aid of μCT and statistical characteristics, *Ceram. Int.*, **39**, 2415 – 2422, (2013).

35 Grothausmann, R., Zehl, G., Manke, I., Fiechter, S., Bogdanoff, P., Dorbandt, I., Kupsch, A., Lange, A., Hentschel, M., Schumacher, G., Banhart, J.: Quantitative structural assessment of heterogeneous catalysts by electron tomography, *J. Am. Chem. Soc.*, **133**, 18161 – 18171, (2011).

36 Roberts, A.P., Garboczi, E.J.: Elastic properties of model porous ceramics, *J. Am. Ceram. Soc.*, **83**, 3041 – 3048, (2000).

[37] Zhao, F., Landis, H.R., Skerlos, S.J.: Modeling of porous filter permeability via image-based stochastic reconstruction of spatial porosity correlations, *Environ. Sci. Tech*., **39**, 239 – 247, (2006).

[38] Gulati, S.: Thermal stresses in ceramic wall-flow diesel filters. *SAE Technical paper*, 830079, (1983).

[39] Bruno, G., Pozdnyakova, I., Efremov, A.M., Levandovskyi, A.N., Clausen, B., Hughes, D.J.: Thermal and mechanical response of industrial porous ceramics, *Mater. Sci. Forum*, **652**, 191 – 196, (2010).

[40] Stafford, R.J., Golovin, K.B., Dickinson, A., Watkins, T.R., Shyam, A., Lara-Curzio, E.: Comparison of elastic moduli of porous cordierite by flexure and dynamic test methods. In: Advances in bioceramics and porous ceramics V, ed. by Roger Narayan, Paolo Colombo, Michael Halbig, Sanjay Mathur. DOI: 10.1002/9781118217504.ch22.

[41] Bruno, G., Efremov, A.M., Clausen, B., Balagurov, A.M., Simkin, V.N., Wheaton, B.R., Webb, J.E., Brown, D.W.: On the stress-free lattice expansion of porous cordierite. *Acta Mater*., **58**, 1994 – 2003, (2010).

[42] Bruno, G., Efremov, A.M., An, C.P., Nickerson, S.T.: Not all microcracks are born equal: thermal vs. mechanical microcracking in porous ceramics, In Widjaja S, Singh D (Eds), Advances in bioceramics and porous ceramics IV – Ceramic Engineering & Science Proc., 32:137 – 152, (2011).

[43] Görner, W., Hentschel, M.P., Müller, B.R., Riesemeier, H., Krumrey, H., Ulm, G. Diete, W., Klein, U., Frahm, R.: BAMline: The first hard x-ray beamline at BESSY II, *Nucl. Instrum. Meth. A*, **467 – 468**, 703 – 706, (2001).

[44] Rack, A., Zabler, S., Müller, B.R., Riesemeier, H., Weidemann, G., Lange, A., Goebbels, J., Hentschel, M.P., Görner, W.: High resolution synchrotron-based radiography and tomography using hard x-rays at the BAMline (BESSY II), *Nucl. Instrum. Meth. A*, **586**, 327 – 344, (2008).

[45] Lange, A., Hentschel, M.P., Kupsch, A., Müller, B.R.: Numerical correction of x-ray detector backlighting, *Int. J. Mat. Res*., **103**, 174 – 178, (2012).

[46] Kupsch, A., Hentschel, M.P., Lange, A., Müller, B.R.: How to correct x-ray detector backlighting, (in German), *MP Mater. Test*., **55**, 577 – 581, (2013).

[47] Weitkamp, T., Haas, D., Wegrzynek, D., Rack, A.: ANKAphase: Software for single-distance phase-retrieval from inline x-ray phase-contrast radiographs, *J. Synchrotron Rad*., **18**, 617 – 629, (2011).

[48] Schuster, A.: On the investigation of hidden periodicities with application to a supposed 26 day period of meteorological phenomena, *Terr. Magn.*, **3**, 13 – 41, (1898).

[49] Feldkamp, L.A., Davis, L.C., Kress, J.W.: Practical cone-beam algorithm, *J. Opt. Soc. Am. A*, **1**, 612 – 619, (1984).